Optics & Laser Technology 194 (2026) 114495

Contents lists available at ScienceDirect

Optics and Laser Technology

journal homepage: www.elsevier.com/locate/optlastec

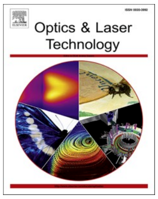

The influence of different core-ring intensity distributions on the capillary shape and resulting weld in laser welding of steel[☆]

Felix Zaiß[a,*], John Powell[a], Michael Haas[a,f], Johannes Wahl[a], Christian Diegel[b], Klaus Schricker[b], Jean Pierre Bergmann[b], Marc Hummel[c,d], Christoph Spurk[d], Alexander Olowinsky[c], Felix Beckmann[e], Julian Moosmann[e], Christian Hagenlocher[a], Thomas Graf[a]

[a] *Institut für Strahlwerkzeuge (IFSW), University of Stuttgart, Pfaffenwaldring 43, 70569 Stuttgart, Germany*
[b] *Production Technology Group, Technische Universität Ilmenau, Gustav-Kirchhoff-Platz 2, 98693 Ilmenau, Germany*
[c] *Fraunhofer-Institute for Laser Technology ILT, Steinbachstraße 15, 52074 Aachen, Germany*
[d] *RWTH Aachen University, Chair for Laser Technology LLT, Steinbachstraße 15, 52074 Aachen, Germany*
[e] *Institute of Materials Physics, Helmholtz-Zentrum Hereon, Max-Planck-Str. 1, 21502 Geesthacht, Germany*
[f] *Graduate School of Excellence Advanced Manufacturing Engineering, University of Stuttgart, Nobelstr. 12, 70569 Stuttgart, Germany*

ARTICLE INFO

Keywords:
Laser welding
Capillary
Weld seam
High-speed synchrotron
X-ray imaging
Beam shaping
Multi-core fiber system
Spatter formation
High-speed imaging

ABSTRACT

Laser welding was carried out using a co-axial core-ring beam, with independent control of the power to the core and the ring. The welding process was observed using high-power X-rays and high-speed imaging equipment. Adjusting the relative powers of the core and the ring beams was found to have profound effects on the shape of both the capillary created and the weld melt pool. Moderate laser power densities in the ring were found to increase the top diameter of the weld pool and reduce fluctuations in the welding process. High laser power densities in the ring led to the creation of a second capillary which largely acted independently of the capillary generated by the laser power in the core. At high power densities and welding speeds the two capillaries were almost completely separated in the direction of travel.

1. Introduction

Steel, due to its high weight-to-strength ratio and low cost [1], is used in the automotive sector in crash-relevant areas [2]. Recent applications include its use in electric vehicles for battery frame to enhance safety during crashes [3,4]. The joining of shells and the housings of battery cells and electronics, by means of laser welding are generally one of the final steps in the manufacturing processing chain and requires defect-free welds to avoid damage to internal components manufactured in previous processing steps [5].

One major defect during the laser welding process of steel is the detachment of melt droplets (spatter) [6,7], resulting in under-filling, which reduces the mechanical properties of the resulting weld [8,9]. At high welding velocities, which are desired for economic productivity, the formation of spatter increases during the laser welding process [10].

The underlying mechanisms of spatter formation are, as described in [6,7,11], an upward melt flow leading to the detachment of spatter, if the kinetic energy of the melt particle is at least greater than the surface tension and the kinetic energy of the spatter. This acceleration is caused from adverse flow field conditions in the melt pool and friction effects of exhausted metal vapor from the laser induced capillary [12–14].

To address the flow field conditions, a change in the size of the melt pool and the melt pool cross sections in aluminium [15] and steel [16] could be achieved by means of a second laser to reduce the melt flow velocities aside the capillary [10,17]. To address vapor friction effects, crucial geometric properties of the capillary like its opening diameter [18,19] and its inclination angle in relation to the material surface [11,14,20] could be adjusted to reduce the formation of spatter. Additionally, the mechanical properties of the material like surface tension of the liquid are also of major significance, and can be influenced by the

---

☆ This article is part of a special issue entitled: 'LaserEMobility' published in Optics and Laser Technology.

* Corresponding author.
E-mail address: felix.zaiss@ifsw.uni-stuttgart.de (F. Zaiß).

https://doi.org/10.1016/j.optlastec.2025.114495
Received 10 April 2025; Received in revised form 22 October 2025; Accepted 30 October 2025
Available online 13 December 2025

ambient atmosphere and its pressure [13,21–23].

While previous solutions have proven effective, they often involve a high degree of complexity and implementation effort, highlighting the need for simpler and more practical approaches.

As one of the more recent developments in the field of laser material processing, beam shaping technologies provide significant potential for optimizing laser welding processes. One way of creating a specific beam shape or intensity distribution on the sample's surface is to use two separate, superimposed laser beams. This approach has been found to influence the formation of spatter [15,16], but, with regard on setup and adjustment, are also impractical for industrial use. Another way of creating superimposed intensity distributions is to use dual-core fibers [24] which transmit laser beams in a core waveguide and a surrounding ring waveguide. These systems create a ring-shaped intensity distribution around a Gaussian or top-hat intensity distribution in the center. The use of such a core-ring intensity distributions can influence various aspects of the welding process, e.g. the formation of spatter [25,26]. It has also been noted that the shape of the capillary changes as the power ratio between the core and ring fiber output changes [18]. However, the early versions of this technology in [18,25,26] are limited, as the power in the core and ring fiber cannot be controlled independently. Multi-core fiber systems that deliver adjustable amounts of laser power to the central core and to the surrounding ring component of the fiber [27], are therefore of major interest and are the subject of this present investigation. In order to use these systems effectively the utilisation of such beam shaping tools needs to be better understood.

Bespoke core-ring intensity distributions can be used to change the laser-material interaction in deep-penetration welding processes [28]. For example, a change in the geometry of the melt pool, such as an increase in its width, can influence the melt flow within the melt pool around the capillary [17].

Previous work using such systems has shown an influence on the melt pool's geometry in aluminium with increasing ring power [29] and demonstrated that the geometry of the capillary and the weld's cross-section can be adapted by the core-ring intensity distributions when welding steel [30].

With regards to metallographic influence, core-ring intensity distributions spread laser power input to a larger area, which reduces lateral temperature gradients and cooling rates [31]. These changes result in different solidification conditions that refines the grain structure in aluminum, influencing cracking susceptibility [32,33]. When applied to stainless steel grain refinement effects [34] due to the reduction of temperature gradients could be observed, which lead to an improvement in weld properties by a reduction of post-weld deformations [35]. Also, with changes in cooling rates [36], different grain morphologies could be observed, with changes in tensile properties of the material [37,38]. Depending on laser power and welding speed, different levels of grain morphologies were achieved resulting in changes in hardness and fracture strength [39]. Beneficial effects on weld bead characteristics, when using core-ring intensity distributions were observed from as well [30].

The literature presented above shows that the link between spatter and melt and vapour flows has been well investigated. Both, melt and vapor flows, are strongly connected with the shape of the capillary and the melt pool. Core-ring beam shapes are influencing the formation of spatter by influencing both, as they can affect the shape of the capillary and the shape of the melt pool. The hypothesis of this work is, that the effect of the ring can be adjusted so that it shapes the weld pool, the capillary or both. The threshold for influencing the capillary shape should be connected with a local temperature increase exceeding evaporation temperature. In order to prove this hypothesis, we holistically analyse by synchrotron X-ray imaging the capillary shape and metallographic sections for the melt pool shape. The comparison of these geometric quantities with the number of produced spatters identifies the beneficial core-ring distributions that reduces spatter and provides causal link on how core-ring beam shapes influence the welding process of stainless steel.

This study looks into how different core-ring power distributions affect the geometry of laser generated capillary in AISI304 (DIN X5CrNi18-10, 1.4301) stainless steel, and thus influence the geometry of the melt pool and the quality of the eventual weld in terms of spatter formation at welding speeds of 3 and 12 m/min.

The X-ray images show for the first time the creation of a secondary, separated capillary from the ring beam at high welding speeds and gain new insights in the interaction between core-ring beam shapes, capillary shape and spatter formation. At low welding speeds, the X-ray images show the beneficial effects of ring beam, which creates a secondary capillary connected to the capillary created from the core beam, to significantly reduce spatter formation. With reduced ring beam intensity, additional melting occurs, which affects primarily melt pool shape and reduces the formation of spatter, for both welding speeds investigated.

2. Experimental setup

A schematic of the experimental setup used is shown in Fig. 1. The samples, made of 2 mm thick AISI 304 (DIN X5CrNi18-10, 1.4301) stainless steel, were cut to a 100 mm by 30 mm format, the sides were milled and cleaned. The sample was held in a clamping device mounted on a sled that can move in the x-direction with speeds in excess of 20 m/min. A moving sample and a stationary laser beam enabled an investigation by means of high-speed X-ray videos of the welding process. A bead-on-plate welding arrangement was set up, whereby the side surface of the individual 2 mm thick sheet metal was welded, assuming that this is a perfect fit-up example of a weld between two sheets.

The laser system consisted of a "Highlight FL 4000CSM-ARM" fiber laser from Coherent, that generates a beam with a wavelength of 1070 nm. To deliver the laser power to the processing optics, a fiber with a concentric ring-core wave-guiding structure consisting of a core with a diameter $d_{f,core}$ of 25 μm and a surrounding ring with an inner diameter $d_{f,ring,in}$ of 100 μm and an outer diameter $d_{f,ring,out}$ of 170 μm was used. The power in the core and ring waveguides of the fiber could be controlled independently and this made it possible to generate a range of ring-core intensity distributions on the surface of the sample, as described in [29]. In this case, the laser power could reach up to 1500 W in the core, and 2500 W in the ring. Using a 150 mm collimation lens and a 400 mm focusing lens (Fig. 1 (2)), the optical system produced the focussing characteristics given in Table 1.

The X-ray imaging system in the beamline P07 EH4 of PETRA 3 at Deutsches Elektronen-Synchrotron (DESY) in Hamburg was used to observe the shape of the capillary during the welding process [40], the collimated X-ray beam exits the shielding tube see Fig. 1 (3), passes through the sample and is absorbed by it to varying degrees, depending on the local thickness and the density of the material. The high brilliance of the X-ray beam facilitates the observation of phase contrasts in the material, both at the liquid–gas phase boundary of the capillary, and the liquid–solid phase boundary of the melt pool [41,42]. A detailed description of the experimental setup is also shown in [43].

A GaGG:Ce scintillator crystal with a thickness of 1.6 mm was placed behind the sample to convert the attenuated X-ray beam, with an energy of 74 keV, into visible light. The illuminated back side of the scintillator was then recorded by a high-speed camera (i-SPEED 727 from iX Cameras), see Fig. 1 (4), at a framerate of 10 kHz and a spatial resolution of 390 pixel/mm. To protect the electronics of the camera from the X-ray radiation, a mirror was used to keep the camera out of the X-ray beam path.

Additionally, to record the generation of spatter during the welding process, a high-speed camera (OS8 from IDT Vision) fitted with a Navitar zoom lens and a short pass filter at 950 nm, was used. The camera was positioned perpendicular to the welding direction and tilted at 9° relative to the sample's surface (see Fig. 1 (5)). In order to observe the rapidly moving, small spatter particles and their trajectory, the camera's frame rate was configured at 8 kHz and the spatial resolution

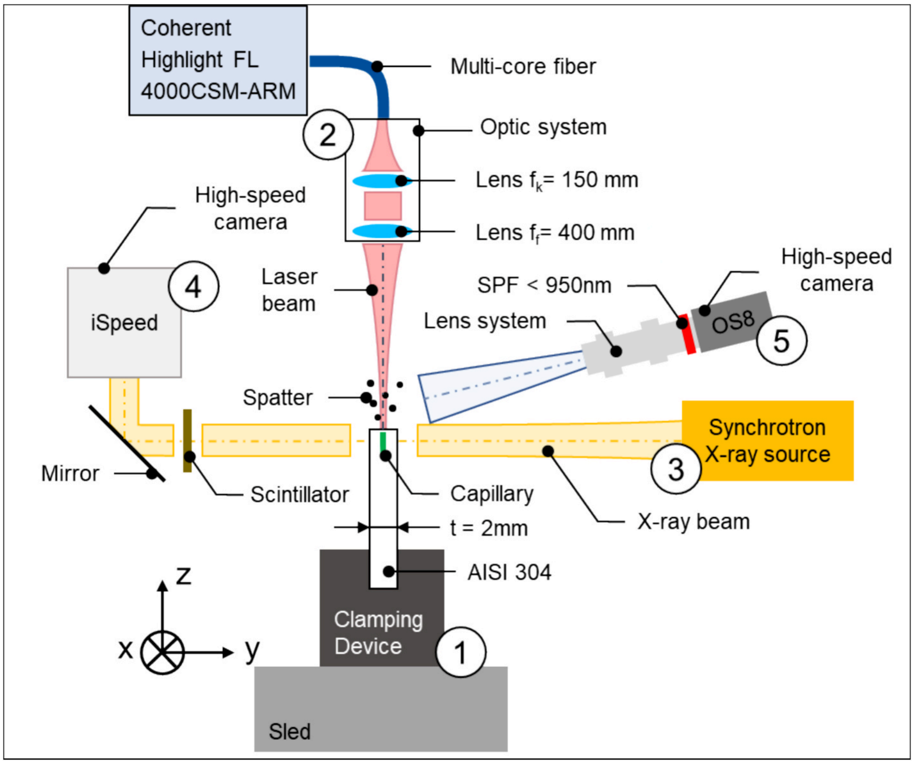

Fig. 1. Schematic of the experimental setup. 1. Sample and clamping device on sled, moving in the x-direction (into the page). 2. Optical system with collimation lens $f_k = 150$ mm and focusing lens $f_f = 400$ mm. 3. Synchrotron X-ray beam source. 4. High-speed camera records the shape of the capillary and weld pool (in the direction of travel) during the welding process visualised by the scintillator via a mirror. 5. High-speed camera system capturing the generation of spatter during the welding process.

Table 1
Properties and parameters of the laser beam source and the optical system.

Parameter	Unit	Coherent Highlight FL 4000CSM-ARM
Laser type	–	Fiber laser
Wavelength of laser beam λ	nm	1070
Maximum laser power in core $P_{max,core}$	W	1500
Maximum laser power in ring $P_{max,ring}$	W	2500
Fiber core diameter $d_{f,core}$	µm	25
Fiber ring inner diameter $d_{f,ring,in}$	µm	100
Fiber ring outer diameter $d_{f,ring,out}$	µm	170
Focal length of collimation lens f_k	mm	150
Focal length of focusing lens f_f	mm	400
Focused beam core spot diameter $d_{0,core}$	µm	65
Focused beam ring inner diameter $d_{ring,in}$	µm	263
Focused beam ring outer diameter $d_{ring,out}$	µm	446

was set at 800 pixels/mm.

The core and ring beam profiles at the focus position are shown in Fig. 2, as measured using a Primes "MicroSpotMonitor MSM+" Device. The beam from the fiber‘s core was focused on the sample's surface to a spot diameter of $d_{0,spot}$ 65 µm. The beam from the fiber's ring waveguide was focused to an outer diameter $d_{ring,out}$ of 446 µm and an inner diameter $d_{ring,in}$ of 263 µm, as illustrated in Fig. 2b. Fig. 2c shows a schematic of the beam profile at the focus.

Different power distributions were achieved by varying the laser power in the core and ring fiber for two welding speeds, as listed in Table 2. The main objective of the experiment was to observe welding characteristics at ring-core power ratios of 100:0, 50:50, 20:80 and 0:100, whilst keeping the capillary's penetration depth similar (with an accuracy of ± 0.1 mm) for each speed. In order to increase relevance for laser welding applicators, identical welding depths were achieved for the various power distributions by adjusting the laser power. This was achieved by taking separate X-ray images of power ramps at different power distributions and welding speeds in order to determine the laser power required to achieve the wanted welding depth.

In order to study the Rosenthal and Elongated Capillary regimes as defined by Fabbro [44], two different welding velocities are compared in the framework of this work.

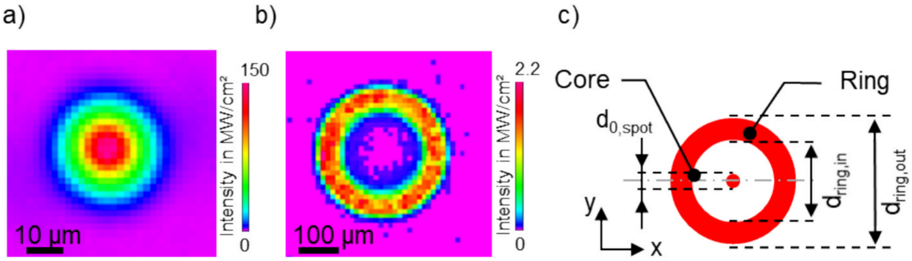

Fig. 2. Measured intensity distributions of ring and core beam at the focus position. (a) Intensity distribution of focused core beam (b) Intensity distribution of focused ring beam (c) Schematic of the beam profile at the focus.

Table 2
Laser powers for different power distributions and welding speeds (C=Core beam, R = Ring beam).

Power distribution and welding speed v_{weld}	100:0 (core beam only)	50:50	20:80	0:100 (ring beam only)
3 m/min, $s_{cap} = 1.3 \pm 0.1$ mm	C: 350 W R: 0	C: 300 W R: 300 W	C: 200 W R: 800 W	C: 0 R: 1250 W
12 m/min, $s_{cap} = 0.85 \pm 0.1$ mm	C: 400 W R: 0	C: 390 W R: 390 W	C: 300 W R: 1200 W	C: 0 R: 2400 W

For the welding speed v_{weld} of 3 m/min the capillary depth s_{cap} was approximately 1.3 mm. In the case of the 12 m/min welding speed, the laser power limit of 2400 W in the ring results in keyhole depths of 0.85 mm (with an accuracy of ±0.1 mm). Table 2 summarises the power levels used in the core (C) and ring (R) of the fiber at the different welding speeds. It is clear that the different power ratios required different total powers to achieve the same weld penetration.

3. Results & discussion

3.1. The effects of different core-ring combinations on capillary shape

3.1.1. Interpretation of the X-ray videos

To compensate for inhomogeneous grey level distribution in the images, the X-ray recordings were post-processed with a flat field correction (FFC), using the average image of 20 frames from the X-ray recording prior to the start of the welding process [45,46].

Fig. 3a shows a time-averaged image of 1000 frames from a flat-field corrected X-ray video, corresponding to a welded length of 2 mm, during welding at 3 m/min and a power distribution of 50:50. The raw image consists of grey values, which correspond to the intensity of the X-ray radiation on the scintillator. At the location of the vapor-filled capillary, the X-rays propagate through less absorbent material, resulting in higher grey values in the images [47], and thus enabling detection of its cross-section. By averaging the grey values of 1000 frames, noise can be reduced and an example of the resulting image is shown in Fig. 3a. For the sake of better visibility of the average dimensions of the melt pool (which is only faintly visible in the grey image) and the capillary, the image in Fig. 3b has been colour-coded by the “mpl-plasma” LUT of the Fiji image processing software [48]. Fig. 3c presents a schematic of a characteristic capillary.

3.1.2. Welding with the core beam only

Fig. 4a and 4b show the schematic images of the averaged X-ray recordings for welding with the core beam only. Dimensionally accurate schematics of this type will be presented in the following sections for improved clarity. Fig. 4c shows the time-averaged X-ray videos from 1000 frames for 3 m/min and Fig. 4d for 12 m/min, from which Fig. 4a and 4b were derived.

The core-only weld at 3 m/min was carried out with 350 W of power in the core beam and 0 W in the ring (Fig. 4a). The 12 m/min core-only weld was carried out at the slightly higher power of 400 W (Fig. 4b). The profile of the laser beam on the sample has been added at scale to the figures.

With a focussed spot diameter of 67 μm on the surface of the sample a narrow, almost straight capillary was formed at both welding speeds, with a slight curvature in the direction of travel in its lower portion. At a welding speed of 3 m/min, shown in Fig. 4a, the width of the capillary (in the direction of travel) varied from 40 μm at the top of the weld, to zero at the bottom and its depth was 1.3 mm. The limited optical resolution and contrast of the captured images allow for the identification of the location of the tip of the capillary with an accuracy of ± 0.1 mm. The lag between the top front face and the bottom (as a result of the curvature) was 28 μm. At a welding speed of 12 m/min (Fig. 4b), the diameter of the capillary varied from 56 μm at the top of the weld to zero at the bottom and its depth was 0.85 mm. The lag between the top front face and the bottom was 51 μm.

3.1.3. 50:50 Core:Ring power distribution

Fig. 5 shows the average shape of the capillaries created at 3 m/min and 12 m/min with the 50:50 power distribution (300 W core, 300 W ring).

In the case of welding at a speed of 3 m/min, the capillary’s depth was 1.3 mm ± 0.1 mm, and its width was 49 μm at the top of the capillary and zero at the bottom. The lag between the top front and bottom was 36 μm. The change of the melt pool’s geometry, compared to Fig. 4a, can clearly be seen. The lower half of the melt pool looks similar to that in Fig. 4a, but the melt is extended in the direction of travel towards the top. This increase of the melt pool’s length can be attributed to the additional ring power on the sample’s surface, which heats up the

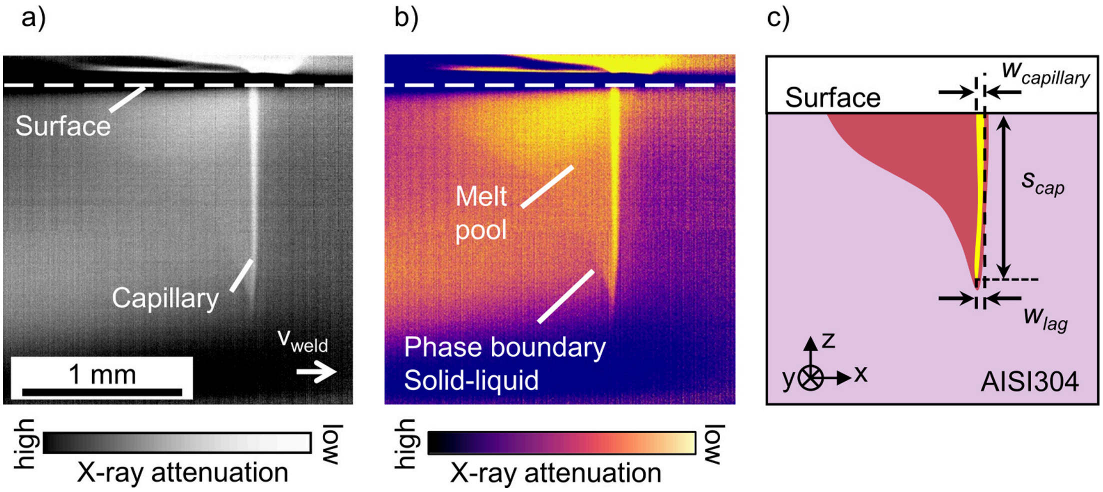

Fig. 3. X-ray imaging. (a) Time-averaged image of an X-ray video sequence from 400 frames with increased contrast for improved visibility of capillary (b) Recolored image for improved visibility of the melt with different zones identified (c) Schematic with characteristic dimensions.

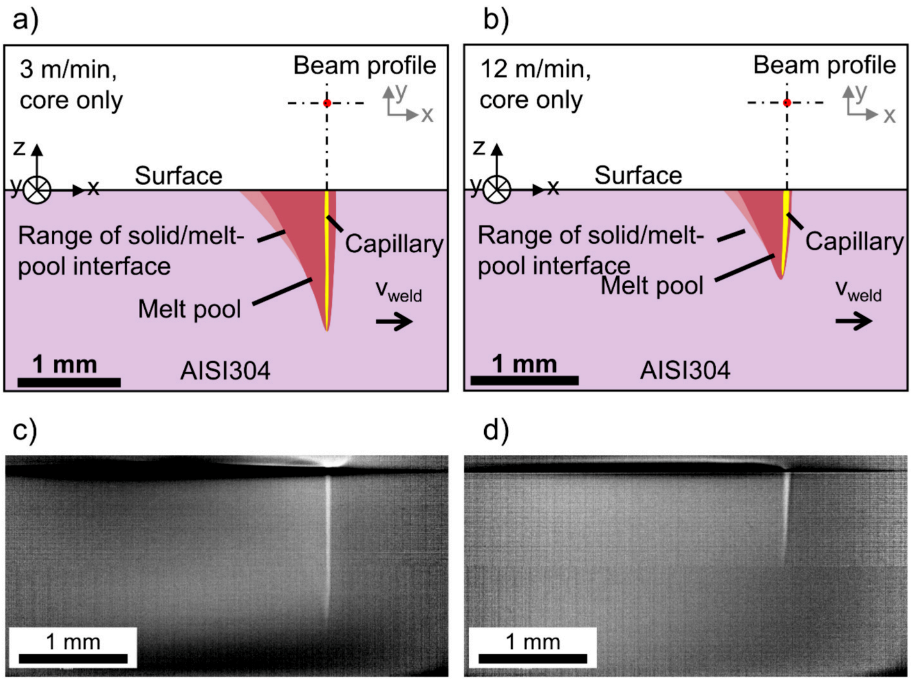

Fig. 4. Schematic representation of the average image from 1000 frames of X-ray video recording when welding with the core beam only (a) 3 m/min and (b) 12 m/min. Original average grayscale image from 1000 frames of X-ray video sequence with increased contrast for (c) 3 m/min and (d) 12 m/min.

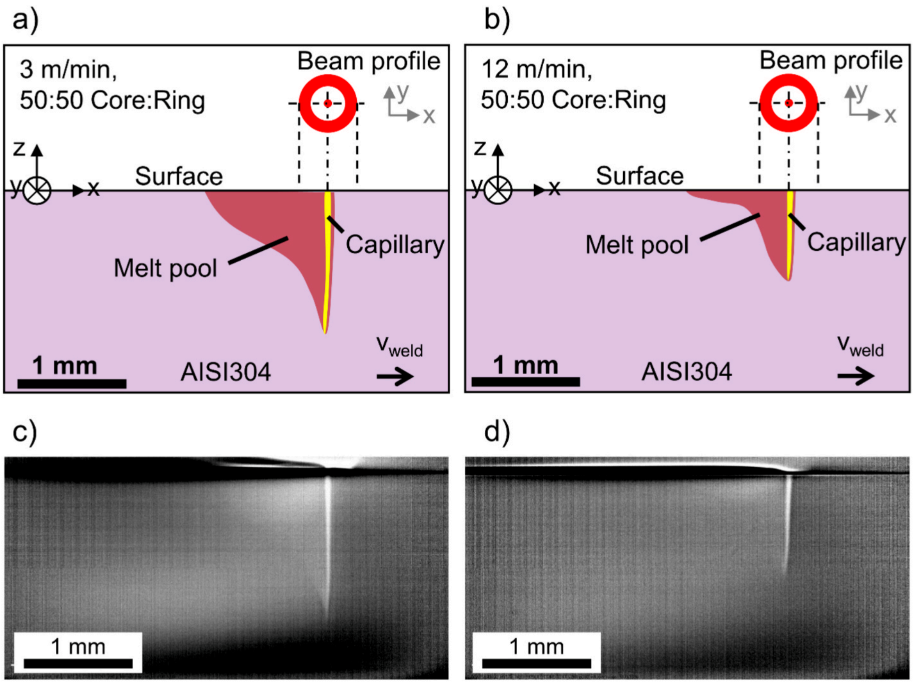

Fig. 5. Schematic representation of the average image from 1000 frames of X-ray video recording when welding with a 50:50 core-ring power distribution at (a) 3 m/min and (b) 12 m/min. Original average grayscale image from 1000 frames of X-ray video sequence with increased contrast for (c) 3 m/min and (d) 12 m/min.

area around the core spot. The ring beam is insufficiently intense to evaporate its own capillary, but melts extra material in the top half of the weld by conduction from the surface. This additional input of energy also reduces the amount of energy required by the core to penetrate to the same depth as the core-only weld from 350 W to 300 W. In the case of the weld at a speed of 12 m/min, the capillary's dimensions were: depth 0.85 mm, top width 48 μm, lag 56 μm (the measurements of the capillary for all cases are summarised in Table 3 below). Fig. 5c shows the raw, time-averaged X-ray videos from 1000 frames for 3 m/min and Fig. 5d for 12 m/min.

3.1.4. 20:80 Core:Ring power distribution

To produce the welds shown in Fig. 6, the power in the core was decreased and the power in the ring was increased to produce a 20:80 power distribution (200 W core, 800 W ring). With this distribution the intensity of the ring-shaped beam was capable of evaporating its own capillary.

In the case of welding at 3 m/min, the additional capillary is wider

Table 3
Capillary dimensions – depth, top width (in the direction of travel), lag.

Power distribution (C:R) and welding speed v_{weld}		100:0	50:50	20:80	0:100
3 m/min	Capillary depth s_{cap} in mm	1.3 ± 0.1	1.3 ± 0.1	1.3 ± 0.1	1.3 ± 0.1
	Top width $w_{capillary}$ in µm	40	49	250	590
	Lag w_{lag} in µm	18	36	20	362
12 m/min	Capillary depth s_{cap} in mm	0.85 ± 0.1	0.85 ± 0.1	0.85 ± 0.1	0.85 ± 0.1
	Top width $w_{capillary}$ in µm	56	48	346	900
	Lag w_{lag} in µm	51	56	46	428

(250 µm at the top) and shallower (610 µm) than the capillary generated by the core beam, and is located behind the latter, see Fig. 6a. The narrow, straight capillary created by the core beam is still visible in the leading, lower half of the combined vapor capillary and, in this area, looks similar to those in Fig. 4 and Fig. 5. Once again, the additional energy from the ring beam has reduced the power in the core beam necessary to achieve the penetration depth of 1.3 mm.

In the case of welding at 12 m/min, shown in Fig. 6b, a phenomenon occurs which might not have been expected. The two capillaries are almost completely separated in the direction of travel. Once this has been noted, the beginnings of this separation can also be seen in the result obtained at 3 m/min presented in Fig. 6a. As we shall discuss later in this paper, the independence of the two capillaries is also evident in the cross sections of the weld seams. This separation effect is also visible in the time-averaged X-ray images from 1000 frames for 3 m/min as shown in Fig. 6c and for 12 m/min as shown in Fig. 6d.

The separation of the two capillaries means that there is a liquid zone between the two, which can be seen very clearly in Fig. 6b and 6d. Because of its position between two capillaries, this liquid zone is subjected to the evaporation pressure and the upwards thrust of ejected vapour on both its leading and trailing faces. As will be seen later, if the liquid zone extends upwards, close to the workpiece surface (as in Fig. 6b and 6d), this double thrust results in the generation of a considerable amount of spatter.

3.1.5. *Ring-shaped laser beam only*

The average shapes of the capillaries created by the ring alone (1250 W) can be seen in Fig. 7. At the sample's surface the size of the capillary's opening (590 µm in the direction of travel) was increased significantly compared to those of previously presented samples. It is also clear that the front and back walls of the capillary are curved and the whole capillary is tilted in the direction of movement. These trends are even more pronounced in the case of the welding at a speed of 12 m/min (capillary's opening 900 µm in the direction of travel). Fig. 7c shows the time-averaged X-ray videos from 1000 frames for 3 m/min and Fig. 7d for 12 m/min.

In the case of the 3 m/min, and to a lesser extent at 12 m/min, the shape of the melt pool at the bottom differs significantly from the shapes shown in the previous Figures. In the previous beam configurations, there was very little melt directly behind the bottom of the capillary and almost none below it. In the 3 m/min case the broader, higher power heat source has resulted in a noticeable amount of melting taking place in the vertical direction after the passage of the capillary. A possible explanation for this is suggested by the geometry of the capillary, which would support a considerable amount of beam reflection off the front face of the capillary onto the rear wall. This heating of the rear wall could then lead to further melting of the workpiece behind the capillary.

The 12 m/min ring-only case (Fig. 7b) is the only example amongst these results where the capillary is considerably longer (in the direction of welding) than the laser beam. This phenomenon has been explained in detail in [49]. This lateral extension of the capillary is due to the existence of high (supercritical) melt flow rates around the sides of the capillary. Very high flow rates are to be expected in the 12 m/min ring-only case because both the weld and capillary are unusually broad in

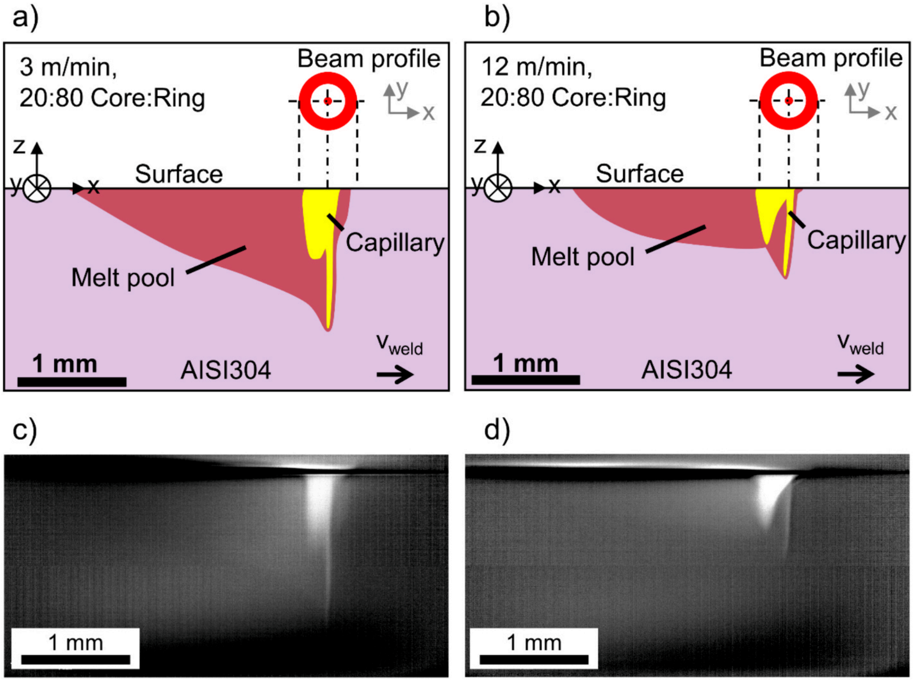

Fig. 6. Schematic representation (top) of average image from 1000 frames of X-ray video recording when welding with a 20:80 core-ring power distribution at (a) 3 m/min (b) 12 m/min. Original average grayscale image from 1000 frames of X-ray video sequence with increased contrast for (c) 3 m/min and (d) 12 m/min.

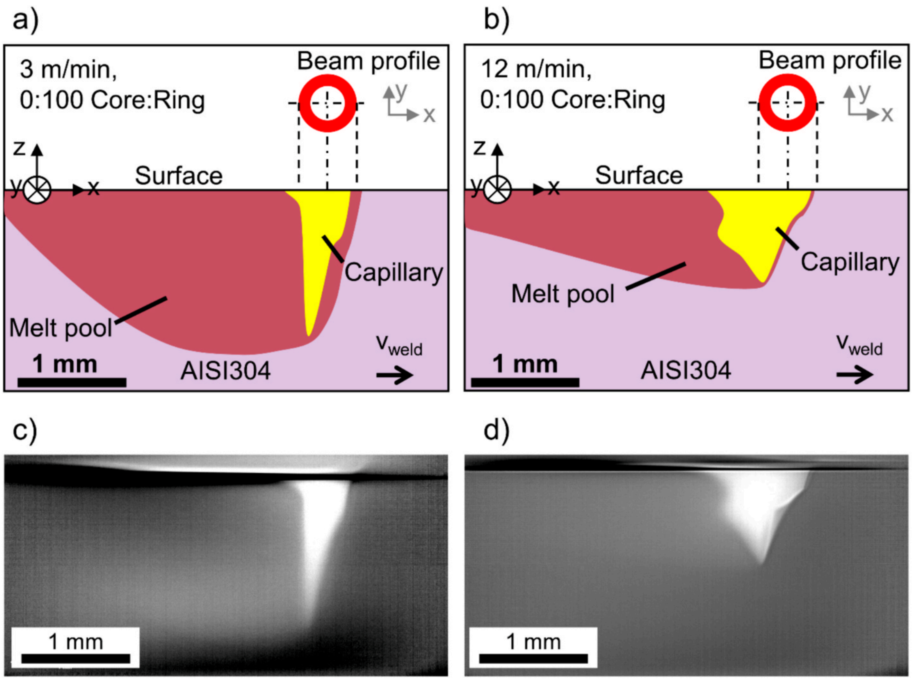

Fig. 7. Schematic representation of the average image from 1000 frames of X-ray video recording when welding with the ring-shaped beam only at (a) 3 m/min (b) 12 m/min. Original average grayscale image from 1000 frames of X-ray video sequence with increased contrast for (c) 3 m/min and (d) 12 m/min.

cross-section (i.e. perpendicular to the weld direction). A broad weld involves a large volume of melt, and a broad capillary constricts the channels through which that liquid must flow.

3.2. Effect of different core-ring combinations on cross section of welded seam

To investigate the influence of different core-ring intensity distributions on the resulting weld, lateral cross sections of the welded seams were made. Sections were taken 10 mm from the beginning of the welds and these were polished and adler-etched [50] to visualize the weld. The prepared cross-sections were examined with a digital stereo-microscope with a "AxioCam MRc5" from Zeiss at 50x magnification.

Fig. 8 presents the cross sections of the seams produced at 3 m/min and the measurements taken from the images are given in Table 4. It should be noted that the melt pool widths are measured perpendicular to the welding direction, whereas capillary widths are measured parallel to the welding direction. When welding with power only in the core beam, the seam had a narrow, triangular cross section, see Fig. 8a. At the sample's surface, the width of the melt pool w_{melt} was measured to be 373 μm and the melt pool reached to a depth of $s = 1430$ μm into the sample, resulting in an aspect ratio s/w_{melt} of 3.83. The cross-sectional area A_{melt} of the seam was 0.3 mm^2.

With a 50:50 power distribution, see Fig. 8b, the weld pool broadens in the upper part with a width of 488 μm on the top, the lower half, which reaches to a depth of 1433 μm still exhibits the narrow shape obtained with the core beam only. This gives an aspect ratio of 2.94 with a total area A_{melt} of 0.366 mm^2. The increase of width and area are the result of the additional ring beam and the increase in total incident laser power.

When increasing the laser power in the ring further to a 20:80 core-ring power distribution, the weld seam changes from a simple triangular cross section, see Fig. 8c. On top the melt pool's width increased to 704 μm while the melt pool depth was 1407 μm, reducing the aspect ratio to 2. Furthermore, the cross-sectional area A_{melt} of the seam increased significantly to 0.712 mm2. The most important point about this cross section is that it gives an indication that two separate capillaries produced two distinguishable solidification structures. The lowest 25 % of the seam is typical of the lowest region of a weld with only a core beam, see Fig. 8a. Above this zone the solidification pattern is more typical of one related to a much broader capillary, in this case the one created by the ring-shaped beam, which lags behind the capillary generated by the core beam. (As will be seen later, this 'double capillary/double weld' phenomenon is even more pronounced at the higher welding speed of 12 m/min).

Fig. 8d shows the cross section of the weld seam created with the ring-only configuration. The depth of the seam was increased in this case compared to the other samples, see Table 4, even though the capillary's penetration depth was lower. As discussed in section 3.1.5, this increase in the melt depth was probably the result of continued melting after the

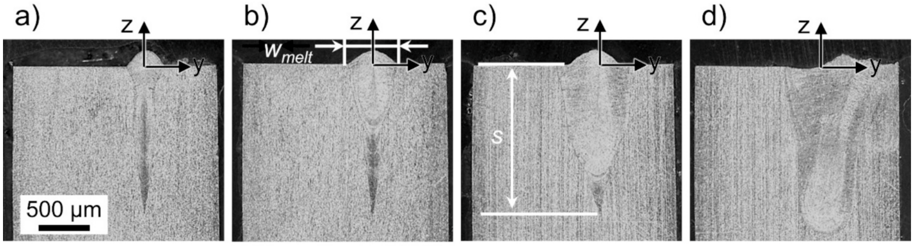

Fig. 8. Cross section of the welded samples with different core-ring intensity distributions at a welding speed of 3 m/min. (a) Core-only (b) 50:50 power distribution (c) 20:80 power distribution (d) Ring-only.

Table 4
Weld seam characteristics when welding at 3 m/min with different core-ring power distributions.

Power distribution at 3 m/min	100:0 C: 350 W R: 0	50:50 C: 300 W R: 300 W	20:80 C: 200 W R: 800 W	0:100 C: 0 R: 1250 W
Melt pool width w_{melt} in µm	373	488	704	961
Melt pool depth s in µm	1430	1433	1407	1640
Aspect ratio s/w_{melt}	3.83	2.94	2	1.7
Area A_{melt} in mm^2	0.3	0.37	0.71	1.1
Joining efficiency J_{eff} v_{weld} •s/P_{Laser} in mm^2/W•s	204	119	70.35	65.6
Melting efficiency M_{eff} v_{weld} •A_{melt}/P_{Laser} in mm^3/(W•s)	0.043	0.031	0.036	0.044

passage of the capillary. The aspect ratio in this case was 2.

Please note that for this cross section, the proximity of the right-hand side of the weld pool to the edge of the sample (see Fig. 8d) has led to a certain amount of heat accumulation, which has increased the width of the melt on that side.

The results of the measurements and the analysis of the cross-sections are summarized in Table 4. The Joining efficiency J_{eff} referred to in the table is a measure of what area of join would be created per unit of total laser energy used between two components if these were not bead-on-plate welds. The melting efficiency M_{eff} is a measure of the volume of melt created per unit of total incident laser energy used.

The same investigations of the cross-sections of the welded samples were made for the welding speed of 12 m/min and the results are shown in Fig. 9. When welding with power in the core beam only, a narrow, triangular cross section is observed, see Fig. 9a, which is very similar to, but not as deep as, the cross section observed at 3 m/min in Fig. 8a. The width of the seam was measured to be 276 µm and the depth was 850 µm, resulting in an aspect ratio of 3.08. The irregular looking sides of the seam cross section suggest an unstable liquid flow and instability of the capillary, which will be the subject of further research by the present authors.

It is clear from Fig. 9b that, when using the 50:50 power distribution, the weld pool width broadens towards the top, resulting in a measured width at the top of the melt pool of 447 µm. Thus, the influence of the additional ring beam on the geometry of the melt pool is clearly visible. This increase in the melt pool's width can give rise to a decrease in the gradients of the melt flow velocity around the capillary near the sample's surface. The liquid in front of the capillary flows through the channels between the side walls of the capillary and the sides of the melt pool, towards the back of the melt pool [17]. The maximum melt flow velocity at any vertical position in the melt pool depends on the local width of the channel and the welding velocity [51]. In this case, as a first approximation, an increase in melt pool width at the sample's surface by the factor of 1.62, with a similar capillary shape (compare Fig. 9a and 9b), would reduce the maximum melt flow velocity by approximately 27 %, according to [17]. The depth of the melt pool was measured to be 930 µm, giving an aspect ratio of 2.08.

Fig. 9c shows that, when using the 20:80 power distribution, the melt pool broadened to 615 µm at the sample's surface. The melt pool depth was measured to be 845 µm. This depth could be reached due to the core beam creating the lower melt profile, which looks similar to those seen in Fig. 9a and 9b. In this case the 'double capillary/double weld' phenomenon discussed above is very pronounced. This is an important result as, without the insight obtained with the aid of X ray video monitoring, it might have been assumed that the core and the ring laser beams act one within the other to produce a combined capillary in a common melt pool. In fact, particularly at high speeds, it can be seen that the core beam creates its melt pool before the capillary generated by the ring beam comes into play.

The ring-only laser welding process at 12 m/min (see Fig. 9d) generated a broad (791 µm wide, 924 µm deep) weld seam as would be expected from the size of the capillary. As with the result obtained at 3 m/min for the ring-only configuration, there is evidence of secondary absorption of the reflected beam by the rear wall of the capillary, giving rise to some secondary melt generation after the laser itself has passed by.

Melting efficiency and joining efficiency

Table 3 and Table 4 reveal similar trends in the melting and joining efficiencies achieved by the various power combinations.

The single power source combinations (100 % core or 100 % ring) have higher melting efficiencies than the mixed combinations (50:50 or 80:20). This is because the ring power input in the two mixed combinations is not intense enough to generate an almost instantaneous capillary in the material, and therefore all, or most, of the ring laser beam hits the surface of the (molten or solid) workpiece at approximately normal incidence (compare Fig. 5 and Fig. 6 with Fig. 7). This interaction results in a single absorption/reflection event and a large proportion of the ring-shaped beam's power is reflected away from the welding zone in this area. This is in contrast to what happens inside a capillary, where there are multiple reflections of the beam, which is therefore absorbed more effectively. The increase in beam absorption in a capillary results in higher melting efficiencies.

Joining efficiency is a function of maximum melt depth, welding speed and laser power, and is of primary interest to welding production engineers. In all the cases reviewed here the core-only weld had the highest joining efficiency. This is clearly because, if the majority of the laser power is involved in creating a deep, narrow capillary, the weld depth per Watt of laser beam power will be maximised. However, weld quality is also a prime concern of welding production engineers. In the case of these experiments there were differences between the magnitude

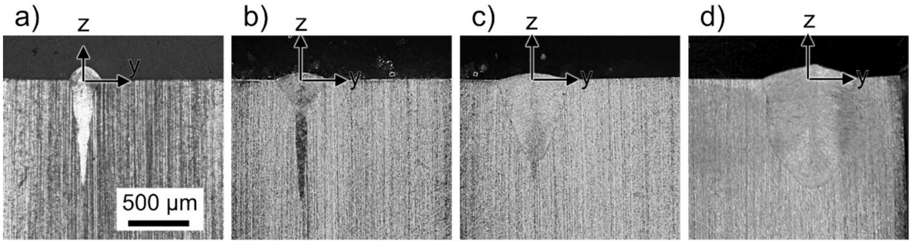

Fig. 9. Cross section of the welded sample with different core-ring intensity distributions at a welding speed of 12 m/min. (a) Core-only (b) 50:50 power distribution (c) 20:80 power distribution (d) Ring-only.

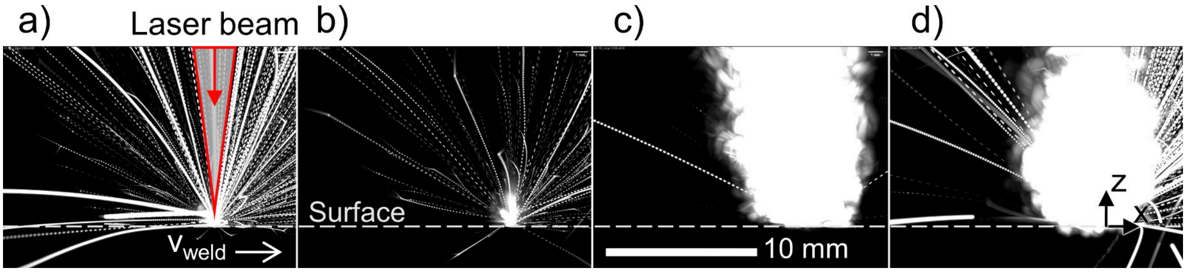

Fig. 10. Generation of spatter as maximum grey value images from 2000 frames at a welding speed of 3 m/min. (a) Core-only (b) 50:50 power distribution (c) 20:80 power distribution (d) Ring-only.

of the fluctuations in penetration depth between the welding processes, with the core-only welds at 12 m/min being the least stable. This complex matter of weld process stability for core-only and 50:50 core-ring power distributions has been the subject of additional work by the present authors [52].

3.3. Effect of different core-ring combinations on spatter generation

One indicator of welding quality and efficiency is the level of spatter generation from the process. Spatter particles are made up of small liquid droplets ejected from the melt pool next to the capillary entrance (see Fig. 10) and this material ejection has a negative effect on weld quality. High-speed imaging was therefore used for this investigation to monitor the spatter produced for each set of welding parameters. The settings and orientation of the high-speed camera were as described in Fig. 1. To visualize the overall generation of spatter, the maximum pixel values of each image were overlayed. The overlayed video sequence corresponds to a welding distance of 10 mm, which equates to 2000 frames at a speed of 3/min, and 400 frames at a speed of 12 m/min. The videos were taken after the process achieved steady state conditions.

Fig. 10 shows the overlayed image for a welding speed of 3 m/min with the relevant core-ring power configurations from Table 2. The welding direction was towards the right in these photos (i.e. the material was moving towards the left). Fig. 11 shows similar images for the 12 m/min welding process. In Fig. 10c and 10d and Fig. 11c and 11d the overall optical brightness of the vapour plume above the welds caused considerable over-exposure of the images. However, several spatter-related observations can be drawn from these images.

i. Spatter generation (per unit length of weld) increases with welding speed over the parameter range employed here. This is probably the result of increased melt velocities in within the weld pool [7].
ii. Core-ring power combinations which result in double, or greatly extended capillaries lead to the generation of large amounts of vapour. This is probably due to the significantly increased evaporating surface.
iii. A comparison of the core-only and the 50:50 distribution indicates that the addition of a ring source which extends the melt without creating an additional capillary, can reduce spatter.
iv. The 20:80 results suggest that the creation of a secondary capillary generated by the ring broadens the capillary zone in the direction of welding, which can suppress spatter at low speeds. At higher speeds however, the two capillaries can separate, and a large amount of spatter is generated. A probable source of much of this spatter is the liquid zone separating the two capillaries (see Fig. 6).
v. The ring-only results indicate that, under the parameters used here, a large amount of vapour is generated, and a reduction of spatter formation compared to the core-only configuration.

The recordings were analysed and the number of spatter were counted automatically from a particle tracking software Trackpy [53], identifying and counting individual spatter from image sequences. Three sections of each recording were selected for evaluation, each corresponding to a welding distance of 10 mm; the number of images was adjusted accordingly.

Fig. 12 shows the amount of spatter ejected per mm of welding distance. The bar plots represent the average number of spatters observed in the three sections, while the error bars indicate the maximum and minimum values.

At a welding speed of 3 m/min (50 mm/s), most spatter are generated with the core-only with an average of 19.1 spatter per mm, followed by the ring-only power distribution. The fewest spatter were

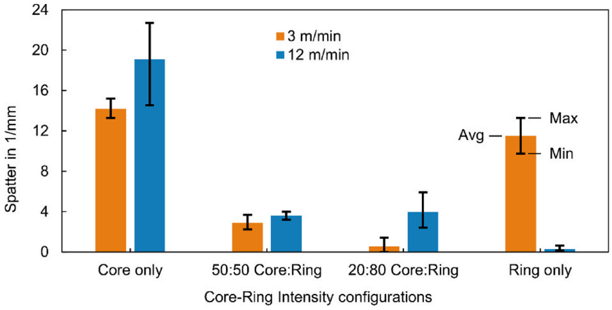

Fig. 12. Spatter per mm welding distance for different core-ring intensity distributions and welding speeds. The individual bar height represents the average value, and the error bars represent the maximum and minimum values of spatter per mm from three sections of the recordings.

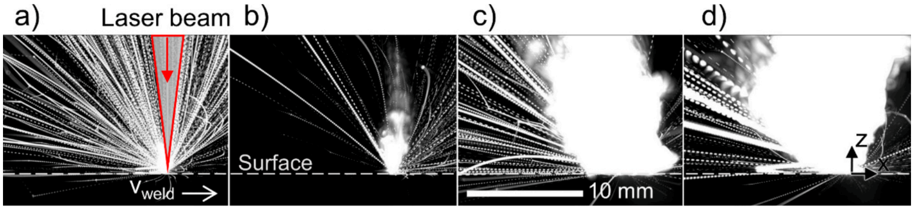

Fig. 11. Generation of spatter as maximum grey value images from 500 frames at a welding speed of 12 m/min. (a) Core-only (b) 50:50 power distribution (c) 20:80 power distribution (d) Ring-only.

Table 5
Weld seam characteristics and efficiencies for different core-ring power distributions at 12 m/min welding speed.

Power distribution (C:R) at 12 m/min	100:0 C: 400 W R: 0	50:50 C: 390 W R: 390 W	20:80 C: 300 W R: 1200 W	0:100 C: 0 R: 2400 W
Melt pool width w_{melt} in µm	276	447	615	791
Melt pool depth s in µm	850	930	846	924
Aspect ratio s/w_{melt}	3.08	2.08	1.37	1.17
Area A_{melt} in mm^2	0.109	0.133	0.284	0.579
Joining efficiency J_{eff} $v_{weld} \bullet s/P_{Laser}$ in mm^2/(W•s)	426	238	112	78
Melting efficiency M_{eff} $v_{weld} \bullet A_{melt}/P_{Laser}$ in mm^3/(W•s)	0.055	0.034	0.038	0.048

generated at a power distribution of 20:80 C:R with an average of 0.5 spatter per mm over a distance of 30 mm.

At a welding speed of 12 m/min (200 mm/s), most spatter are generated with the core-only power distribution, with an average of 14.1 spatter per mm. Fewest spatter were generated at a power distribution of ring-only, with an average of 0.3 spatter per mm over a distance of 30 mm. At a power distribution of 50:50C:R an average of 3.6 spatter per mm were counted, similar to an average of 3.9 spatter per mm with the 20:80C:R power distribution.

Reduction of spatter from pre-heating effects from ring beam, as at the 50:50C:R power distribution, help reduce fluctuation in laser absorption rates, hence preventing strong vapor exhaustions which reduces to spatter formation [54].

At slow feed rates, a ring beam at 20:80 increases the capillary aperture significantly. As a result, vapor from the previous narrow capillary generated by the core beam interacts less with the capillary back at the top. This reduces friction effects and decreases spatter.

At high feed rates, a ring beam at 20:80 provides no benefits. In this case, the capillaries are separated and do not act together, leaving a narrow capillary. Consequently, vapor friction effects remain. However, there is still a reduction in spatter due to preheating effects as with 50:50C:R. The least number of spatter were counted in the configuration with ring only power configuration, only here the rear wall of the capillary is inclined, see Fig. 7. This tilt reduces vapor friction effects on the capillary back wall as described in [11,20]. However, high laser power requirements and low joining efficiency, see Table 5, make this process inefficient from a productivity point of view.

4. Conclusions

From the results presented here one can draw the following conclusions:

Independently controlled core-ring laser combinations offer a powerful tool in weld process control.

In cases where the ring laser energy density is too low to create a capillary, the ring-shaped laser beam acts as a pre- and post- heating assist to the core beam. (The level of melting associated with this the pre- and post- heating is dependent upon the energy density and the process speed.) Under these conditions the two laser beams can act together in creating a weld which has a broader melt pool towards the top of the weld. This reduces spatter formation for both low and high welding speeds.

If sufficiently high-power densities in the ring beam are employed, the ring beam and the core beam can form individual capillaries which are progressively separated from each other in the direction of welding as speeds are increased, and which can effectively act independently from each other. The resulting weld can show evidence of this ‘double weld’ effect. At low welding speeds the capillaries act together and vapor friction effects at the capillary back are reduced, as a result, spatter formation is supressed. At high welding speeds, the capillaries from the core and ring beam separate, and a further reduction in vapour friction effects on the capillary rear wall cannot be achieved. However, the advantages of preheating remain, which contribute to a reduction in spatter formation.

The separation of the capillaries created from the ring and core beam at high welding speeds and laser power in the ring, could be shown for the first-time using synchrotron X-ray imaging.

When welding at high welding speeds with the ring-only beam configuration, the back wall of the capillary tilts, affecting vapour friction effect and reduces spatter formation at the expense of high laser power and low joining efficiency.

Welding with combined core-ring laser beams demands significantly more power than a single focused beam for the same weld depth and speed, whereas optimizing core-ring dimensions and power distribution can enhance efficiency, stability, and reduce spatter formation.

4.1. Outlook

Future work will expand on these findings through detailed metallographic analyses to quantify grain sizes within the weld and heat-affected zones, thereby enabling a deeper understanding of microstructural development under different beam profiles. In addition, tensile tests will be performed on welded samples to directly correlate mechanical performance with the measured microstructural features and capillary geometries. These complementary investigations will provide a more comprehensive framework for linking laser beam intensity distribution to weld integrity, thereby providing information for the design of process parameters for high-performance steel welding.

Future work will cover the analytical description of the formation of the secondary capillary, in order to determine a parameter-based threshold, as well as the influence of capillary geometry on the vapor flow and how it affects spatter formation.

CRediT authorship contribution statement

Felix Zaiß: Writing – original draft, Visualization, Methodology, Investigation, Formal analysis, Data curation, Conceptualization. **John Powell:** Writing – review & editing, Validation, Supervision, Methodology, Conceptualization. **Michael Haas:** Writing – review & editing, Software, Methodology, Data curation. **Johannes Wahl:** Writing – review & editing, Validation, Conceptualization. **Christian Diegel:** Writing – review & editing, Data curation. **Klaus Schricker:** Writing – review & editing. **Jean Pierre Bergmann:** Writing – review & editing. **Marc Hummel:** Writing – review & editing, Data curation. **Christoph Spurk:** Writing – review & editing, Data curation. **Alexander Olowinsky:** Writing – review & editing, Project administration. **Felix Beckmann:** Data curation. **Julian Moosmann:** Data curation. **Christian Hagenlocher:** Writing – review & editing, Validation, Supervision, Methodology, Conceptualization. **Thomas Graf:** Writing – review & editing, Supervision, Methodology.

Declaration of competing interest

The authors declare that they have no known competing financial interests or personal relationships that could have appeared to influence the work reported in this paper.

Acknowledgements

The presented work was funded by the Deutsche Forschungsgemeinschaft (DFG, German Research Foundation) – 503306266.

(Partially) Supported by the InnovationCampus Future Mobility funded by the Baden-Württemberg Ministry of Science, Research and the Arts.

The presented investigations were carried out within the cooperation “Laser Meets Synchrotron” (www.laser-meets-synchrotron.de). The experimental setup and its operation were funded by the Deutsche Forschungsgemeinschaft e.V. (DFG, German Research Foundation) within the framework of the Collaborative Research Centre SFB1120-236616214 “Bauteilpräzision durch Beherrschung von Schmelze und Erstarrung in Produktionsprozessen”. The experiments were carried out in cooperation with Helmholtz-Zentrum Hereon in Hamburg at Beamline P07 of DESY PETRA III as part of proposal BAG-20211050 and we would like to thank F. Beckmann, J. Moosmann and all people involved for their support.

References

[1] University of Cambridge, Material Selection and Processing, Department of Engineering (2002). http://www-materials.eng.cam.ac.uk/mpsite/ (accessed December 17, 2024).

[2] A. Jambor, M. Beyer, New cars — new materials, Mater. Des. 18 (1997) 203–209, https://doi.org/10.1016/S0261-3069(97)00049-6.

[3] S. Lindner, Stainless steel in traction battery housings, ATZ Worldw 121 (2019) 64–67, https://doi.org/10.1007/s38311-018-0227-0.

[4] Steel battery housings, Thyssenkrupp (n.d.). https://www.thyssenkrupp-steel.com/en/industries/automotivetrucks/e-mobility/battery-housing/ (accessed February 25, 2025).

[5] P. Stavropoulos, K. Sabatakakis, H. Bikas, Welding challenges and quality assurance in electric vehicle battery pack manufacturing, Batteries 10 (2024) 146, https://doi.org/10.3390/batteries10050146.

[6] S.M. Robertson, A.F.H. Kaplan, J. Frostevarg, Material ejection attempts during laser keyhole welding, J. Manuf. Process. 67 (2021) 91–100, https://doi.org/10.1016/j.jmapro.2021.04.052.

[7] A.F.H. Kaplan, J. Powell, Spatter in laser welding, J. Laser Appl. 23 (2011) 032005, https://doi.org/10.2351/1.3597830.

[8] Y. Ai, P. Jiang, C. Wang, G. Mi, S. Geng, W. Liu, C. Han, Investigation of the humping formation in the high power and high speed laser welding, Opt. Lasers Eng. 107 (2018) 102–111, https://doi.org/10.1016/j.optlaseng.2018.03.010.

[9] S. Katayama, Fundamentals and Details of Laser Welding, Springer Singapore, Singapore, 2020. Doi: 10.1007/978-981-15-7933-2.

[10] F. Nagel, L. Brömme, J.P. Bergmann, Effects of two superimposed laser beams on spatter formation during laser welding of high alloyed steel, J. Laser Appl. 31 (2019), https://doi.org/10.2351/1.5040572.

[11] Y. Kawahito, K. Nakada, Y. Uemura, M. Mizutani, K. Nishimoto, H. Kawakami, S. Katayama, Relationship between melt flows based on three-dimensional X-ray transmission in-situ observation and spatter reduction by angle of incidence and defocusing distance in high-power laser welding of stainless steel, Q. J. Jpn. Weld. Soc. 34 (2016) 239–248, https://doi.org/10.2207/qjjws.34.239.

[12] J. Weberpals, F. Dausinger, Fundamental understanding of spatter behavior at laser welding of steel, in: International Congress on Applications of Lasers & Electro-Optics, Laser Institute of America, 2008: p. 704, doi: 10.2351/1.5061334.

[13] V. Rominger, P. Berger, H. Hügel, Effects of reduced ambient pressure on spattering during the laser beam welding of mild steel, J. Laser Appl. 31 (2019), https://doi.org/10.2351/1.5007186.

[14] J.-P. Weberpals, P. Krueger, P. Berger, T. Graf, Understanding the influence of the focal position in laser welding on spatter reduction, International Laser Safety Conference (2011) 159–168, https://doi.org/10.2351/1.5062230.

[15] A. Trautmann, Bifocal hybrid laser welding: a technology for welding of aluminium and zinc-coated steels, Herbert Utz Verlag, München, 2009.

[16] F. Nagel, L. Brömme, J.P. Bergmann, Description of the influence of two laser intensities on the spatter formation on laser welding of steel, Procedia CIRP 74 (2018) 475–480, https://doi.org/10.1016/j.procir.2018.08.147.

[17] M. Beck, Modellierung des Lasertiefschweißens, Teubner, Stuttgart, 1996.

[18] M. Jarwitz, J. Lind, R. Weber, T. Graf, N. Speker, P. Haug, Investigation of the influence of superimposed intensity distributions on the spatter behavior in laser welding of steel using online x-ray diagnostics, in: AIP Publishing, 2018. Doi: 10.2351/7.0004024.

[19] D. Wu, X. Hua, L. Huang, F. Li, Y. Cai, Observation of the keyhole behavior, spatter, and keyhole-induced bubble formation in laser welding of a steel/glass sandwich, Weld World 63 (2019) 815–823, https://doi.org/10.1007/s40194-019-00710-7.

[20] J. Weberpals, F. Dausinger, Influence of inclination angle on spatter behavior at welding with lasers of strong focusability, in: International Congress on Applications of Lasers & Electro-Optics, Laser Institute of America, Orlando, Florida, USA, 2007: p. 1602. Doi: 10.2351/1.5061015.

[21] V. Rominger, T. Harrer, S. Keßler, H. Braun, F. Dorsch, F. Abt, M. Jarwitz, A. Heider, R. Weber, T. Graf, Formation mechanism of process instabilities and strategies to improve welding quality, in: International Congress on Applications of Lasers & Electro-Optics, Laser Institute of America, 2012: pp. 565–573. https://pubs.aip.org/lia/liacp/proceedings-abstract/ICALEO/2012/565/375541 (accessed October 27, 2024).

[22] C. Diegel, T. Mattulat, K. Schricker, L. Schmidt, T. Seefeld, J.P. Bergmann, P. Woizeschke, Interaction between local shielding gas supply and laser spot size on spatter formation in laser beam welding of AISI 304, Appl. Sci. 13 (2023) 10507, https://doi.org/10.3390/app131810507.

[23] L. Schmidt, K. Schricker, J.P. Bergmann, C. Junger, Effect of local gas flow in full penetration laser beam welding with high welding speeds, Appl. Sci. 10 (2020) 1867, https://doi.org/10.3390/app10051867.

[24] Trumpf, Laser welding without spatter?, 2024 https://www.trumpf.com/en_INT/solutions/applications/laser-welding/low-spatter-welding-with-beam-formation-technology/ (accessed November 1, 2024).

[25] N. Speker, P. Haug, S. Feuchtenbeiner, T. Hesse, D. Havrilla, BrightLine weld-spatter reduced high speed welding with disk lasers, in: High-Power Laser Materials Processing: Applications, Diagnostics, and Systems VII, Vol. 10525, SPIE, 2018, pp. 99–104, https://doi.org/10.1117/12.2287205.

[26] F. Kaufmann, A. Maier, J. Schrauder, S. Roth, M. Schmidt, Influence of superimposed intensity distributions on weld seam quality and spatter behavior during laser beam welding of copper with green laser radiation, J. Laser Appl. 34 (2022) 042008, https://doi.org/10.2351/7.0000771.

[27] Coherent, Adjustable Ring Mode (ARM) Faserlaser – HighLight FL-ARM, 2023. https://www.coherent.com/de/lasers/fiber/highlight-fl-arm.

[28] T. Florian, K. Schricker, C. Zenz, A. Otto, L. Schmidt, C. Diegel, H. Friedmann, M. Seibold, P. Hellwig, F. Fröhlich, F. Nagel, P. Kallage, M. Buttazzoni, A. Rack, H. Requardt, Y. Chen, J.P. Bergmann, Combining in situ synchrotron X-ray imaging and multiphysics simulation to reveal pore formation dynamics in laser welding of copper, Int. J. Mach. Tool Manuf. 204 (2025) 104224, https://doi.org/10.1016/j.ijmachtools.2024.104224.

[29] S. Hollatz, M. Hummel, M. Lach, A. Olowinsky, A. Gillner, C. Häfner, F. Beckmann, J. Moosmann, Influence of ring-shaped laser beam during welding of AW-5083 and AW-6082, in: High-Power Laser Materials Processing: Applications, Diagnostics, and Systems XII, SPIE, 2023: pp. 80–89. Doi: 10.1117/12.2649092.

[30] M. Mohammadpour, L. Wang, F. Kong, R. Kovacevic, Adjustable ring mode and single beam fiber lasers: a performance comparison, Manuf. Lett. 25 (2020) 50–55, https://doi.org/10.1016/j.mfglet.2020.07.003.

[31] S. Jabar, T. Sun, P. Franciosa, H.R. Kotadia, D. Ceglarek, B. Paolini, R. Faulhaber, Effect of a ring-shaped laser beam on the weldability of aluminum-to-hilumin for battery tab connectors, J. Laser Appl. 35 (2023) 042038, https://doi.org/10.2351/7.0001156.

[32] V.V. Pamarthi, T. Sun, A. Das, Q. Hayat, A. Griffiths, L. Johnson, P. Franciosa, Tailing and axisymmetric static laser beam shapes to steer microstructure and improve mechanical properties of autogenously laser welded AA6082 alloy, Mater. Des. 250 (2025) 113619, https://doi.org/10.1016/j.matdes.2025.113619.

[33] P. Schempp, M. Rethmeier, Understanding grain refinement in aluminium welding: Henry Granjon Prize 2015 winner category B: materials behaviour and weldability, Weld World 59 (2015) 767–784. Doi: 10.1007/s40194-015-0251-2.

[34] W. Xie, H. Tu, K. Nian, D. Zhang, X. Zhang, Microstructure and mechanical properties of flexible ring mode laser welded 304 stainless steel, Opt. Laser Technol. 174 (2024) 110563, https://doi.org/10.1016/j.optlastec.2024.110563.

[35] S.-H. Choi, J.-H. Kim, H.-W. Choi, Ring beam modulation-assisted laser welding on dissimilar materials for automotive battery, J. Manufact. Mater. Process. 9 (2025) 28, https://doi.org/10.3390/jmmp9020028.

[36] M.J. Sohrabi, H. Mirzadeh, S. Sadeghpour, R. Mahmudi, Grain size dependent mechanical behavior and TRIP effect in a metastable austenitic stainless steel, Int. J. Plast 160 (2023) 103502, https://doi.org/10.1016/j.ijplas.2022.103502.

[37] S. Patra, Sk.Md. Hasan, N. Narasaiah, D. Chakrabarti, Effect of bimodal distribution in ferrite grain sizes on the tensile properties of low-carbon steels, Mater. Sci. Eng. A 538 (2012) 145–155. Doi: 10.1016/j.msea.2011.12.114.

[38] M. Naghizadeh, H. Mirzadeh, Effects of grain size on mechanical properties and work-hardening behavior of AISI 304 austenitic stainless steel, Steel Res. Int. 90 (2019) 1900153, https://doi.org/10.1002/srin.201900153.

[39] E.R.I. Mahmoud, H. Almohamadi, A. Aljabri, M.A. Elkotb, A study on the Fiber YAG laser welding of 304L stainless steel, Metals 11 (2021) 2022, https://doi.org/10.3390/met11122022.

[40] N. Schell, A. King, F. Beckmann, T. Fischer, M. Müller, A. Schreyer, The high energy materials science beamline (HEMS) at PETRA III, MSF 772 (2013) 57–61, https://doi.org/10.4028/www.scientific.net/msf.772.57.

[41] T.E. Gureyev, S.C. Mayo, D.E. Myers, Ya. Nesterets, D.M. Paganin, A. Pogany, A. W. Stevenson, S.W. Wilkins, Refracting Röntgen's rays: propagation-based x-ray phase contrast for biomedical imaging, J. Appl. Phys. 105 (2009), https://doi.org/10.1063/1.3115402.

[42] Y. Kawahito, H. Wang, In-situ observation of laser manufacturing with X-ray technique, Synchrotron Radiat. News 32 (2019) 14–19, https://doi.org/10.1080/08940886.2019.1582283.

[43] F. Kaufmann, C. Forster, M. Hummel, A. Olowinsky, F. Beckmann, J. Moosmann, S. Roth, M. Schmidt, Characterization of vapor capillary geometry in laser beam welding of copper with 515 nm and 1030 nm laser beam sources by means of in

situ synchrotron X-ray imaging, Metals 13 (2023) 135, https://doi.org/10.3390/met13010135.

[44] R. Fabbro, Melt pool and keyhole behaviour analysis for deep penetration laser welding, J. Phys. D Appl. Phys. 43 (2010) 445501, https://doi.org/10.1088/0022-3727/43/44/445501.

[45] J.A. Seibert, J.M. Boone, K.K. Lindfors, Flat-field correction technique for digital detectors, in: J.T. Dobbins Iii, J.M. Boone (Eds.), San Diego, CA, 1998, p. 348, Doi: 10.1117/12.317034.

[46] F. Abt, M. Boley, R. Weber, T. Graf, X-ray videography for investigation of capillary and melt pool dynamics in different materials, in: International Congress on Applications of Lasers & Electro-Optics, Laser Institute of America, Orlando, Florida, USA, 2011, pp. 179–186, Doi: 10.2351/1.5062233.

[47] F. Abt, M. Boley, R. Weber, T. Graf, G. Popko, S. Nau, Novel X-ray system for in-situ diagnostics of laser based processes – first experimental results, Phys. Procedia 12 (2011) 761–770, https://doi.org/10.1016/j.phpro.2011.03.095.

[48] J. Schindelin, I. Arganda-Carreras, E. Frise, V. Kaynig, M. Longair, T. Pietzsch, S. Preibisch, C. Rueden, S. Saalfeld, B. Schmid, J.-Y. Tinevez, D.J. White, V. Hartenstein, K. Eliceiri, P. Tomancak, A. Cardona, Fiji: an open-source platform for biological-image analysis, Nat. Methods 9 (2012) 676–682, https://doi.org/10.1038/nmeth.2019.

[49] E.N. Reinheimer, P. Berger, C. Hagenlocher, R. Weber, T. Graf, Supercritical melt flow in high-speed laser welding and its interdependence with the geometry of the keyhole and the melt pool, Int. J. Adv. Manuf. Technol. (2024), https://doi.org/10.1007/s00170-024-13266-8.

[50] G. Petzow, Metallographic etching: techniques for metallography, ceramography, plastography, 2nd ed, ASM International, Materials Park, OH, 1999.

[51] P. Berger, H. Hügel, Fluid dynamic effects in keyhole welding – an attempt to characterize different regimes, Phys. Procedia 41 (2013) 216–224, https://doi.org/10.1016/j.phpro.2013.03.072.

[52] F. Zaiß, M. Haas, J. Powell, J. Wahl, C. Diegel, K. Schricker, J.P. Bergmann, M. Hummel, C. Spurk, A. Olowinsky, F. Beckmann, J. Moosmann, C. Hagenlocher, T. Graf, Reducing capillary depth fluctuations in high-speed laser welding of stainless steel using multi-core laser technology, Procedia CIRP 124 (2024) 413–417, https://doi.org/10.1016/j.procir.2024.08.144.

[53] Trackpy: Fast, Flexible Particle-Tracking Toolkit — trackpy 0.7, (n.d.). https://soft-matter.github.io/trackpy/v0.7/ (accessed October 21, 2025).

[54] J. Li, Y. Wang, P. Jiang, C. Wang, S. Geng, Spatter elimination mechanism and criterion for adjustable ring-mode laser welding of aluminum alloy, Int. J. Heat Mass Transf. 242 (2025) 126812, https://doi.org/10.1016/j.ijheatmasstransfer.2025.126812.